PL-TR-91-2186

Development and Use of Data Analysis Procedures for the CRRES Payloads AFGL-701-2/Dosimeter and AFGL-701-4/Fluxmeter and Application of the Data Analysis Results to Improve the Static and Dynamic Models of the Earth's Radiation Belts

Bronislaw K. Dichter
Frederick A. Hanser

PANAMETRICS, INC.
221 Crescent Street
Waltham, MA 02154

26 July 1991

Scientific Report No. 3

PHILLIPS LABORATORY
AIR FORCE SYSTEMS COMMAND
HANSCOM AIR FORCE BASE, MASSACHUSETTS 01731-5000

"This technical report has been reviewed and is approved for publication"

MICHAEL D. VIOLET, LT, USAF
Contract Manager

E. G. MULLEN
Branch Chief

WILLIAM SWIDER
Deputy Director

This document has been reviewed by the ESD Public Affairs Office (PA) and is releasable to the National Technical Information Service (NTIS).

Qualified requestors may obtain additional copies from the Defense Technical Information Center. All others should apply to the National Technical Information Service.

If your address has changed, or if you wish to be removed from the mailing list, or if the addressee is no longer employed by your organization, please notify GL/IMA, Hanscom AFB, MA 01731. This will assist us in maintaining a current mailing list.

Do not return copies of this report unless contractual obligations or notices on a specific document requires that it be returned.

REPORT DOCUMENTATION PAGE

Form Approved
OMB No. 0704-0188

1. AGENCY USE ONLY (Leave blank)	2. REPORT DATE	3. REPORT TYPE AND DATES COVERED
	26 July 1991	Scientific No. 3

4. TITLE AND SUBTITLE
Development and Use of Data Analysis Procedures for the CRRES Payloads AFGL-701-2/Dosimeter and AFGL-701-4/Fluxmeter and Application of the Data Analysis Results to Improve the Static and Dynamic Models of the Earth's Radiation Belts

5. FUNDING NUMBERS
PE 62101F
PR 7601 TA 20 WU CF

Contract F19628-87-C-0169

6. AUTHOR(S)
Bronislaw K. Dichter
Frederick A. Hanser

7. PERFORMING ORGANIZATION NAME(S) AND ADDRESS(ES)
Panametrics, Inc
221 Crescent Street
Waltham, MA 02154

8. PERFORMING ORGANIZATION REPORT NUMBER

9. SPONSORING/MONITORING AGENCY NAME(S) AND ADDRESS(ES)
Phillips Laboratory
Hanscom AFB, MA 01731-5000

Contract Manager: Lt Mike Violet/PHP

10. SPONSORING/MONITORING AGENCY REPORT NUMBER
PL-TR-91-2186

11. SUPPLEMENTARY NOTES

12a. DISTRIBUTION/AVAILABILITY STATEMENT
Approved for public release;
Distribution unlimited

12b. DISTRIBUTION CODE

13. ABSTRACT (Maximum 200 words)

Results of a calibration of a spacecraft instrument for measuring fluxes of high energy electrons (1 to 10 MeV) in the Earth's radiation belts are presented. Experimental results are supplemented by Monte Carlo calculations of electron transmission and energy deposition in the instrument sensors.

14. SUBJECT TERMS
Spacecraft Instruments, High Energy Electrons Trapped Radiation Belts

15. NUMBER OF PAGES
30

16. PRICE CODE

17. SECURITY CLASSIFICATION OF REPORT	18. SECURITY CLASSIFICATION OF THIS PAGE	19. SECURITY CLASSIFICATION OF ABSTRACT	20. LIMITATION OF ABSTRACT
Unclassified	Unclassified	Unclassified	SAR

Table of Contents

List of Figures

List of Tables

1. INTRODUCTION

The High Energy Electron Fluxmeter (HEEF) is an instrument for the detection and measurement of high energy (1 to 10 MeV) electrons in the Earth's radiation belts. HEEF is part of the scientific instrument package of the CRRES satellite, which was launched on July 25, 1990 into a low inclination (18°), highly elliptical (350 x 36,000 km) orbit. The goal of the CRRES mission is to improve the understanding of the Earth's radiation belts and their effects on space systems. HEEF has operated properly and nearly continuously since its turn on, two days after launch. The only breaks in the operation of the instrument were due to brief turn off periods while the satellite was in a power saving mode during eclipses.

HEEF is designed to measure the high energy electron population in the radiation belts. To date, this population has not been extensively studied experimentally and is poorly understood. Consequently, HEEF data will provide a large, new data base for the testing of current electron behavior models and the development of new ones. In order for this data base to have the maximum utility, the instrument calibration must be thoroughly described and widely accepted. The initial calibration report was published as a Geophysics Laboratory technical report (Ref. 1). Following the launch of CRRES, the calibration data has been thoroughly re-analyzed and compared with extensive Monte Carlo calculations of a mathematical HEEF model. This report contains the results of this work.

HEEF instrument overview is presented, for completeness, in Section 2. The detailed description of the calibration work is in Section 3. Section 4 contains the results of the analysis of the calibration data, results of the computer calculations and their comparison. The report ends with *Section 5, Summary and Conclusions.*

2. INSTRUMENT OVERVIEW

2.1 Mechanical Design

A schematic cross-sectional view of HEEF is shown in Figure 1. A thin (0.006") Be shield is used to stop electrons below 0.14 MeV and protons below 1.3 MeV and prevent them from entering the instrument. There are four active elements in the instrument, two silicon solid state detectors, a Bismuth Germanate (BGO) scintillator and a plastic scintillator anti-coincidence shield. The solid state detectors are 700 μm thick. This choice of thickness represents a compromise between 1000 μm detectors, which would not permit the passage of 1 MeV electrons into the BGO crystal, and 500 μm detectors, for which the mean energy loss by 10 MeV electrons is not sufficiently large to guarantee no noise difficulty problems on a long-term basis. Tungsten collimators are used to shield the detectors from out of aperture particles. The instrument housing was constructed out of magnesium in order to minimize bremstrahlung. Geometrical information about the detectors is summarized in Table 1. Detailed instrument description can be found in Ref. 2.

Table 1 HEEF Detector Information

A) In-Aperture Telescope View

Detector	Collimated Area (cm^2)	Opening Half Angle (degrees)	Geometric Factor (cm^2-sr)
SSDF	0.719	15.6	0.167
SSDB	0.219	7.5	0.012
BGO	0.219	7.5	0.12

B) Omni-Directional View

Detector	W Shield Equivalent (g/cm^2)	Penetrating Proton Energy (MeV)	Geometric Factor (cm^2-sr)
SSDF	20	115	6.06
SSDB	20	115	3.11
BGO	20	115	78.6
Plastic	15	100	525

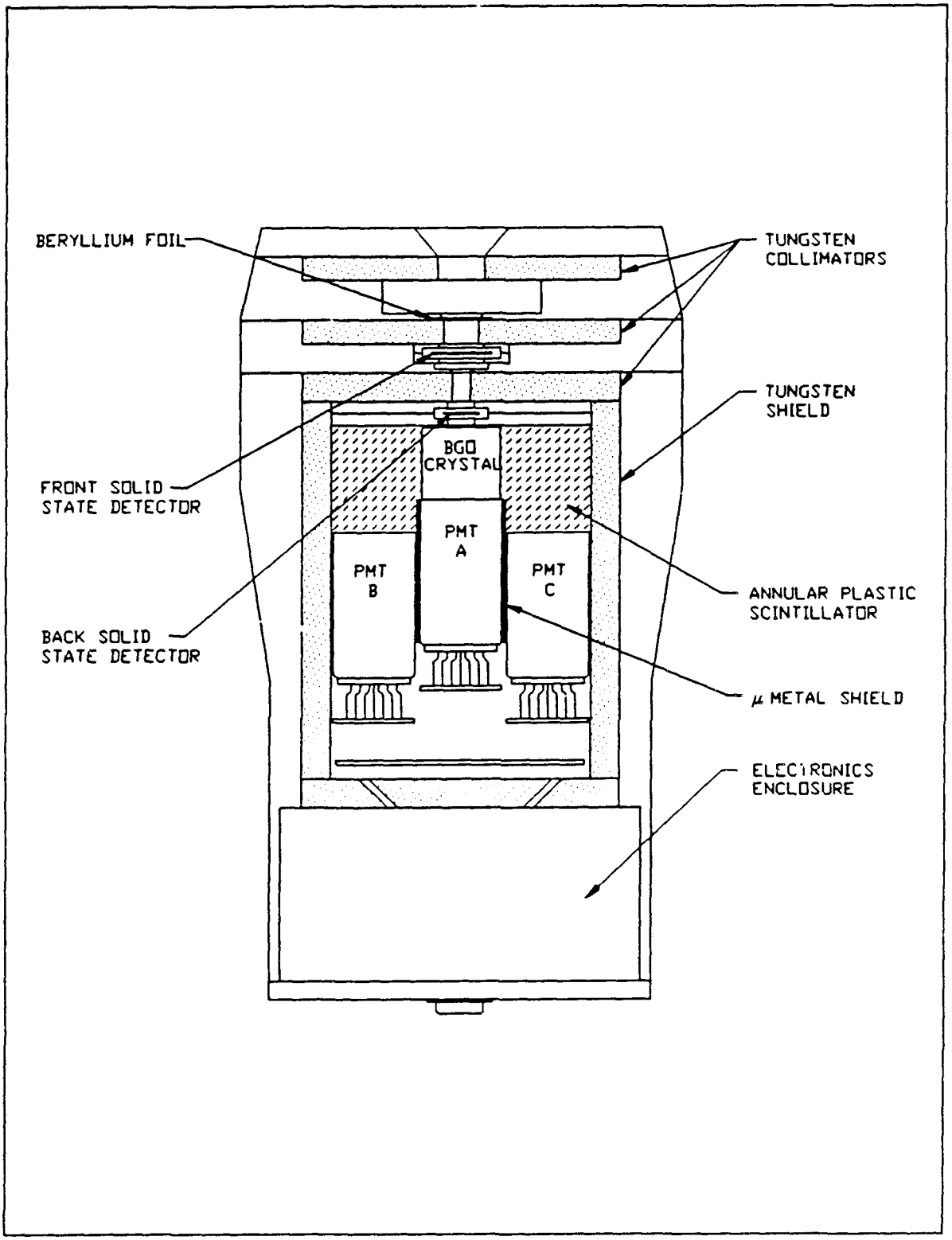

Figure 1 Schematic cross-sectional view of HEEF.

2.2 Electronic Design

HEEF block diagram is shown in Fig. 2. Light pulses from the BGO scintillator are converted to electrical voltage pulses by a photmultiplier tube. The resulting signals are than processed by a pre-amplifier and a shaping amplifier. The amplified BGO pulses are scaled in singles mode, if they exceed the detection threshold. In addition, the BGO signals are pulse height analyzed into one of 10 differential and 1 integral energy ranges if they arrive in coincidence with some combination of the solid state detector signals and the anti-coincidence shield signal. The signals from each of the two solid state detectors, Front (SSDF) and Back (SSDB), are also processed by a pre-amplifier and shaping amplifier. The amplified pulses are scaled in singles mode and are also used as part of the BGO coincidence logic. The plastic scintillator signals, if they exceed a pre-set threshold, are used to veto a BGO event.

The instrument can operate in eight modes, each with different coincidence requirements. The three independent coincidence requirements are CRF (SSDF and BGO), CRB (SSDB and BGO) and ACR (no anti-coincidence shield signal and BGO). Since each condition can be set on or off independently there are eight possible modes. Under normal on-orbit conditions, the instrument operates in a mode with all coincidences enabled (ON/ON/ON mode).

A weak ^{60}Co γ-ray radioactive source, mounted inside the instrument case, provides in-flight calibration information. Since γ-rays cannot generate coincidence signals, data from the source can only be taken with all coincidences disabled (OFF/OFF/OFF mode). Useful calibration data can only be collected when the incident particle flux is low. Typically, this occurs at perigee, when the satellite is underneath the radiation belts, and at apogee when, during quiet times, the spacecraft is outside the belts.

2.3 Principle of Operation

HEEF must be able to detect and measure the energy of incident high energy (1-10 MeV) electrons in the presence of a high energy proton population. Therefore, the instrument must be capable of discriminating against protons to a very high accuracy. This is accomplished by a combination of coincidence requirements and passive and active shielding.

In the normal operating ON/ON/ON mode, a candidate electron event must produce coincident pulses of proper magnitude in SSDF, SSDB and BGO and no pulse in the anti-coincidence shield (coincidence shield pulses are typically due to penetrating out of aperture protons or in-aperture protons that scatter out of the BGO before depositing the full energy in the crystal). The required magnitudes of the various detector pulses were determined by considering electron and proton energy losses in the detectors. In general, protons with energies

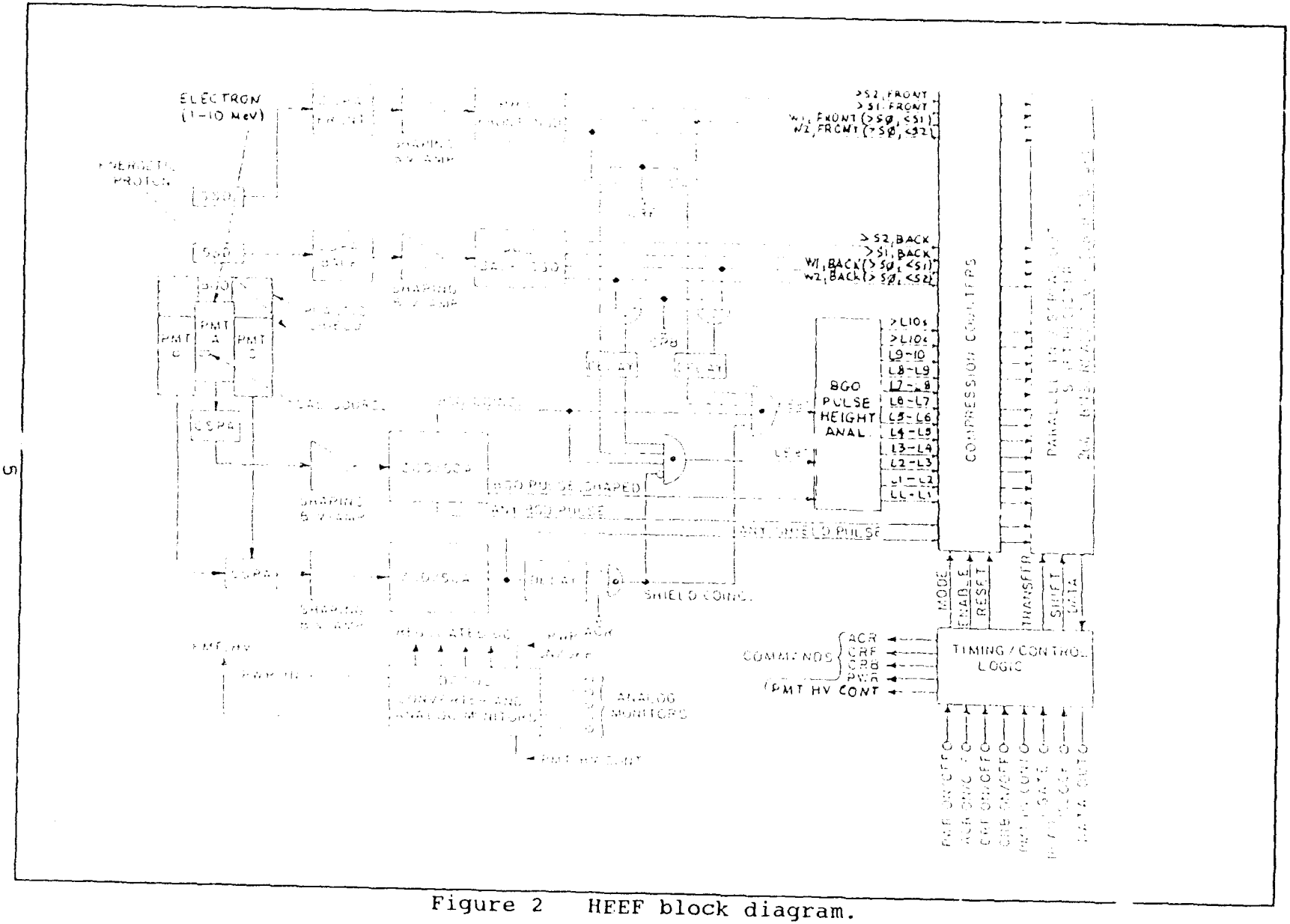

Figure 2 HEEF block diagram.

below about 100 MeV are rejected by their energy loss in the solid state detectors. Protons with energies above 20 MeV are also rejected by their large energy losses in the BGO crystal. As a consequence, there is a region of energies, between 20 and 100 MeV, where in-aperture protons are rejected by two different mechanisms. The omni-directional tungsten shielding is effective up to 140 MeV for protons and to >20 MeV for electrons.

The average energy losses of incident electrons and protons in the HEEF solid state detectors are shown in Figure 3. The thresholds S_o and S_1 form the energy deposition window W1 for the highest energy electrons (2.5 to 10 MeV). W2, the window for lower energy (1 -2.5 MeV) electrons (defined by S_o and S_2), must be widened somewhat because of their larger energy losses. Only very high energy protons, with energies well in excess of 100 MeV can produce pulse heights that fall in the W1 or W2 range. The proton energy loss distributions are not symmetric about the average value but are skewed toward large energy losses. This is a considerable benefit, since it tends to reduce the probability that a proton will lose much less than the average amount of energy. Such a loss could cause it to appear in the electron window, W1 or W2, even if the average loss were above the S_1 and S_2 thresholds. The use of two detectors causes this probability to be much reduced, since it would have to occur in both detectors.

The average energy deposited in the BGO crystal is shown in Figure 3. Electron candidate events are required to have deposited an energy between the LL and L10 thresholds (the differential energy electron channels are listed in Table 2). Penetrating in-aperture protons with energies above 20 MeV will deposit too much energy to be accepted as electron candidates. The use of the L10 threshold on the BGO signal and the S_1 and S_2 thresholds on the solid state detector signals guarantees extreme immunity against in-aperture protons. Penetrating out-of-aperture protons can pass through a corner of the crystal and deposit a smaller amount of energy, within the LL-L10 range, but would produce no coincident solid state detector signals. High energy in-aperture protons can also scatter out of the crystal before depositing their full energy loss and, consequently, meet the LL-L10 limits. In this case, however, there would also be a plastic anti-coincidence shield veto pulse generated, as the scattered proton passed through the plastic scintillator surrounding the BGO crystal.

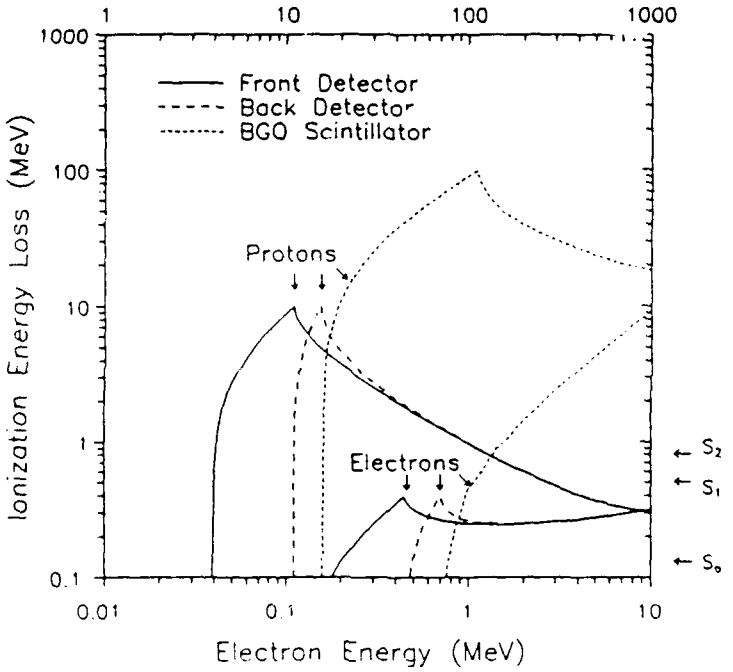

Figure 3 Energy losses of electrons and protons in the HEEF detectors.

Table 2 Electron Channel Properties

Channel Designation	Energy Deposition Range in BGO crystal (MeV)		Incident Electron Energy Range	Channel Geometric Factor
	Minimum	Maximum	(MeV)	(cm^2-sr-keV)
LL-L1	0.44	0.96	1.0 - 1.5	0.186
L1-L2	0.96	1.46	1.5 - 2.0	0.589
L2-L3	1.46	1.96	2.0 - 2.5	1.081
L3-L4	1.96	2.45	2.5 - 3.0	1.349
L4-L5	2.45	2.95	3.0 - 3.5	1.780
L5-L6	2.95	3.44	3.5 - 4.0	2.011
L6-L7	3.44	4.43	4.0 - 5.0	4.784
L7-L8	4.43	5.42	5.0 - 6.0	5.929
L8-L9	5.42	7.41	6.0 - 8.0	11.548
L9-L10	7.41	9.40	8.0 - 10.0	12.302

3. CALIBRATION WORK

3.1 Low Energy Electron Calibration

HEEF response to low energy (0.25 - 1.75 MeV) electrons was measured at the Goddard Space Flight Center (GSFC) electron Van de Graaff accelerator in July 1987 (Ref. 1). In these tests, the instrument was mounted on a rotary motion table inside a vacuum chamber. The table allowed HEEF to be rotated from -21° to +36° with respect to the electron beam. A solid state monitor detector could be moved in and out of the beam, in front of HEEF, to provide beam intensity measurements between HEEF measurement runs. The beam spot size was limited to a circle with an area, A_b, of 1.27 cm^2 by beam line collimators. Prior to placing HEEF in the chamber, a light emitting phosphor illuminated by the beam was used to verify that the beam spot was uniform.

The absolute beam normalization was obtained in the following way. At frequent intervals during the measurements, a monitor detector was moved into the electron beam in front of the HEEF entrance aperture. The sensitive area of the monitor detector was greater than D_b so that if M is the monitor count rate, the average beam intensity at the HEEF entrance aperture, N_e, is given by

$$N_e = \frac{M}{A_b} = 0.787 \cdot M \quad [electrons/(cm^2\text{-}sec)] \tag{3.1}$$

where M is in counts/sec. Beam intensity varied slowly with time, and it was interpolated for times between monitor readings.

The quantity of interest in this test was the effective HEEF geometric factor as a function of electron energy, $GF_e(E)$.

$$GF_e(E) = 2\pi \int A(E,\theta) \cdot \sin(\theta)\, d\theta \tag{3.2}$$

where $A(E,\Theta)$ is the effective HEEF area as a function of electron energy (E) and angle with respect to the beam (Θ). $A(E,\Theta)$ was obtained by measuring the HEEF count rate, $N_{BGO}(E,\Theta)$, and dividing by the (interpolated) absolute beam intensity, $N_e(E)$

$$A(E,\theta) = \frac{N_{BGO}(E,\theta)}{N_e(E)} \quad . \tag{3.3}$$

In practice, eq. (3.2) was evaluated by fitting the measured, discrete $A(E,\Theta)$ values with a smooth cubic spline curve and using this continuous curve in the integrand.

The advantage of the GSFC calibration was that all work was done in vacuum with a

high quality, parallel, mono-energetic, DC electron beam. The interpretation of the data is straightforward and the resulting measured effective areas, $A(E,\Theta)$, are a highly accurate measure of the HEEF response. The drawbacks of this calibration work were that: 1) the beam intensity calibration was not continuous, 2) the beam intensity profile was not accurately measured and 3) the energy range of the Van de Graaff accelerator was limited. The first problem was not serious since the beam intensity did not vary rapidly with time and the interpolation of current measurements to times of interest was sufficiently accurate. The beam profile was determined to be relatively uniform by using the light emitting phosphor. This judgement was supported by electron scattering calculations reported in Section 2.4.2 of Ref. 1. The limited energy range of the GSFC accelerator ($E < 1.75$ MeV) necessitated a second electron calibration at an accelerator capable of reaching higher energies.

3.2 High Energy Electron Calibration

The high energy electron calibration was performed at the Rome Air Development Center (RADC) electron linac at Hanscom AFB. In the linac, electrons were accelerated by the RF electromagnetic fields to energies up to 20 MeV. The beam was then energy analyzed by a 30° bending magnet, penetrated through a beam pipe exit window, travelled through a 1 m air gap and struck HEEF and a nearby monitor detector. Total beam energy loss in traversing the beam pipe exit window and air gap was approximately 1.2 MeV. In practice, the linac produced useful beams with effective energies between 1.3 and 19.8 MeV. HEEF was mounted on a rotary motion table, which enabled rotation out to 24°. A fixed position beam monitor detector was located approximately 10 cm away.

The monitor detector could not be moved in front of the HEEF entrance aperture and therefore could not be used to obtain an absolute beam intensity measurement. This normalization was instead obtained from the total count rate of SSDF (N_{SSDF} = W1 + S1F count rate) with HEEF at 0° with respect to the beam

$$A(E,0°) = 0.719 \frac{N_{BGO}(0°)}{N_{SSDF}(0°)} \quad [cm^2] \qquad (3.4)$$

where N_{BGO} is the BGO crystal counting rate and the effective collimated SSDF area was known to be 0.719 cm^2. As will be seen in Section 4, this procedure had to be modified slightly for some energies. Once HEEF was rotated to non-zero angles, the instrument collimation made the effective SSDF area a complex function of the rotation angle and angular spread in the beam. Therefore, another method was used to tie the non-zero angle measurements to the 0° absolute measurements. The monitor detector did not move as HEEF was rotated, so that it could be used for angle-to-angle normalization. If $M(\Theta)$ is the monitor count rate for a HEEF rotation angle of Θ, then the effective HEEF area, as a function of Θ, is

$$A(E,\theta) = 0.719 \frac{M(0°)}{N_{SSDF}(0°)} \frac{N_{BGO}(\theta)}{M(\theta)} \quad [cm^2] \quad . \qquad (3.5)$$

The advantage of the linac was in the large beam energy range available. There were, however, two significant problems with the linac beams. One problem was that the beam had to travel through a significant amount of degrader material (equivalent to 0.61 g/cm^2 of Al) before striking HEEF. As a result, the electron beam suffered angular scattering and energy straggling. The RF structure of the beam was a second significant problem. The linac was designed to accelerate electrons in traveling wave RF "buckets" which have time widths on the order of the HEEF coincidence circuit time resolution, 1.1 μsec. If more than one particle strikes HEEF, within 1.1 μsec, pile-up and measurement of erroneous pulse heights in the detectors will result. Although much effort was devoted to setting up the linac beam so as to minimize the chances of multiple electrons in RF "buckets", there were times that this was a significant problem. The effects of the problems and their solutions are discussed in Section 4.

3.3 Proton Response Measurements

A key aspect of the HEEF design was the immunity of the instrument to energetic protons. In order to verify the proton rejection capability, HEEF was tested at the Harvard Cyclotron Laboratory (HCL) proton accelerator. The cyclotron generated a 144 MeV primary proton beam, which, by use of degrader material, could be reduced in energy down to 20 MeV. Due to the low intensity of the available proton beam only upper limits of the proton response could be measured for most of the energies studied between 20 and 144 MeV. The results from HCL show that the minimum HEEF proton suppression, in the ON/ON/ON mode, is a factor of 10^4. That is at most 1 proton, out of 10^4 incident, will produce an erroneous valid electron signal. A full discussion of the proton response tests is in Section 5 of Ref. 1.

4. ANALYSIS OF CALIBRATION DATA

4.1 TIGER Code Calculation Description

The validity of the experimental calibration work was checked using a highly realistic computer model of electron transport through solid matter (TIGER code). The TIGER code is a coupled electron/photon Monte Carlo transport comp er code (J. A. Halbleib and T. A. Melhorn, Sandia National Laboratory) which can be used to model instrument responses to electrons. A series of calculations, for the HEEF geometry, were carried out using this program (Ref. 3). In the calculations, electrons, generated at the center of the entrance aperture and initially moving along the axis of the instrument, were followed as they travelled and scattered through the instrument, depositing energy in SSDF, SSDB, BGO crystal or in the collimators. No coincidence requirements were imposed, so that the output of the program consisted of three singles spectra of deposited energy (SSDF, SSDB and BGO crystal) and fractions of incident electrons that strike the three detectors. Various combinations of the calculated values were then used to compare with measured values in order to provide verification of the experimental work.

4.2 Singles Counters - Data and Calculation

The most direct comparison of the measured count rates with the calculated ones can be made with the HEEF singles counters. The ratio of SSDB count rate (W1B+S1B) to the SSDF count rate (W1F+S1F), as a function of incident energy, with HEEF at 0° with respect to the beam, is shown in Figure 4. The calculated values are in excellent agreement with the GSFC data points, obtained using the high quality Van de Graaff beam. Some of the RADC data points are in agreement with the TIGER code values but most are either below or above the calculated curve. The lack of agreement, for the RADC data, is most likely due to the previously mentioned linac beam quality problems. The nature of the problems and the solutions will be discussed in this section.

The points above the calculated curve indicate a larger than expected probability of detecting an electron of a given energy in the back solid state detector. The possibility that a fraction of the electrons has a much higher energy than the nominal beam energy (and thus a higher probability of triggering SSDB) is ruled out by the absence of high energy electron counts in the BGO crystal. In addition, high SSDB/SSDF ratios are also associated with much greater then expected pulse heights in the solid state detectors; S1F/W1F and S2F/W2F ratios are much larger than expected. Since high energy electrons actually deposit less energy in the solid state detectors than low energy ones, this further rules out a high energy contamination of the beam. The experimentally observed signature, however, is exactly what would be expected from electron pile-up events. If two or more electrons strike SSDF, during a time interval shorter than 1.1 μsec, it will lead to a large pulse height in the detector and an enhanced probability that at least one of the electrons will also strike the back detector.

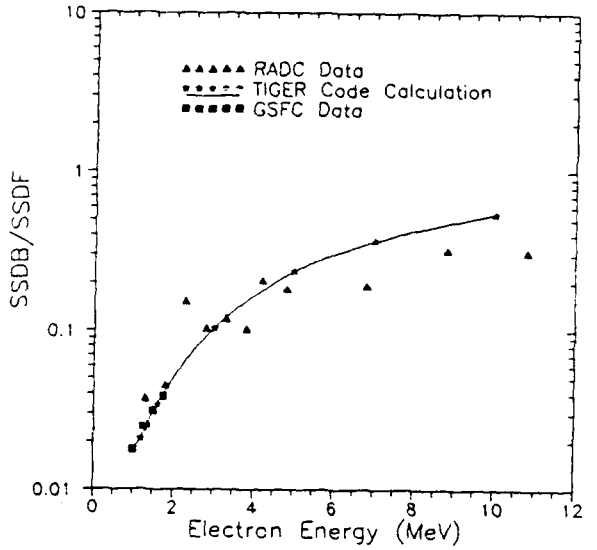

Figure 4 Ratio of solid state detector count rates.

The way to eliminate most of the effects of the pile-up is to normalize the coincidence BGO crystal counts not to the total SSDF counts but to W1F or W2F counts, as appropriate. The reason for this is that events that result in energy depositions within windows W1F or W2F are unlikely to be caused by pile-up events, while the vast majority of the events that result in S1F and S2F signals are pile-up events. In this case, the effective HEEF area, $A(E,\Theta)$, is no longer given by eq. (3.5) but by a modified version of this equation

$$A(E,\theta) = 0.719 \frac{M(0°)}{WnF(0°)} \frac{N_{BGO}(\theta)}{M(\theta)} \quad [cm^2] \qquad (4.1)$$

where WnF is W1F or W2F. Pile-up events must be excluded because the large SSDF and/or SSDB pulse heights will not allow the triple coincidence circuit to record BGO pulse heights for these events, and normalizing to N_{SSDF} = W1F + S1F will lead to an underestimate of $A(E,\Theta)$.

The points under the calculated curve in Figure 4 indicate a lower than expected probability of detecting an electron of a given energy in the back solid state detector. The most likely reason for this effect is the presence of a low energy component in the beam. Since there is no anomalous low energy component in the BGO spectra (E > 1 MeV) at any of the beam energies in question, the low energy component cannot contribute to the effective HEEF area. Therefore, normalizing coincidence BGO counts to N_{SSDF} = W1F + S1F will lead to an underestimate of $A(E,\Theta)$. The proper normalization factor in this case is $f \cdot N_{SSDF}$ where f is the fraction of the total counts that are due to electrons with the nominal beam energy. If we assume that the TIGER code calculated SSDB/SSDF ratio is correct, than the factor f is given by

$$f = R_m / R_c \qquad (4.2)$$

where R_m and R_c are the measured and calculated values of the SSDB/SSDF ratio. Accordingly, eq. (3.5) becomes modified to

$$A(E,\theta) = 0.719 \frac{M(0°)}{f \cdot N_{SSDF}(0°)} \frac{N_{BGO}(\theta)}{M(\theta)} \quad [cm^2] \quad . \tag{4.3}$$

4.3 Coincidence Counters - Data and Calculation

4.3.1 TIGER Code Model

The singles energy deposition spectra and detection probabilities calculated by the TIGER code were used to develop a simple model of the ON/ON/ON HEEF response. In this model, the effective 0° HEEF area, $A_{calc}(E,0°)$, is given by

$$A_{calc}(E,0°) = K \cdot A_F \cdot W_F(E) \cdot W_B(E) \cdot \epsilon \tag{4.4}$$

where A_F is the collimated SSDF area (0.719 cm^2), $W_F(E)$ and $W_B(E)$ are the probabilities that an electron with an energy E will deposit an energy amount within the W1 (or W2 if E < 2.5 Mev) window in the front and back solid state detectors respectively, ϵ is the measured triple coincidence energy (ϵ = 0.64, Ref. 1) and K is an adjustable overall normalization. In the present TIGER code calculations all electrons start at the center of the entrance aperture. Because of angular scattering suffered by the electrons, particles which strike HEEF out away from the center of the aperture will be more likely to be scattered away from the sensitive areas of the detectors. Therefore, a realistic electron distribution will result in a value of K less than 1. A plot of A(E,0°), both calculated and measured, is shown in Figure 4. Given the simplicity of the model the best fit value of K (0.56) is reasonable, and the agreement between the measured and calculated values of A(E,0°) is excellent.

4.3.2 Total Effective Geometric Factor

The HEEF total effective geometric factor, GF(E), is defined by the expression

$$\begin{aligned} GF(E) &= 2\pi \int A(E,\theta) \sin(\theta)\, d\theta \\ &= 2\pi A(E,0°) \int f(E,\theta) \sin(\theta)\, d\theta \end{aligned} \tag{4.5}$$

where $f(E,\Theta) = A(E,\Theta)/A(E,0°)$. The angular distributions $f(E,\Theta)$ are shown in Figure 6.

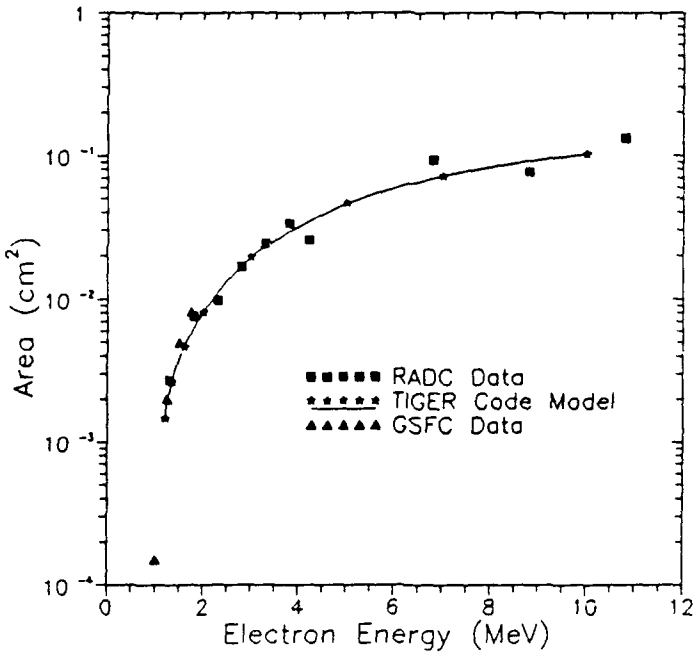

Figure 5 Total effective HEEF 0° area.

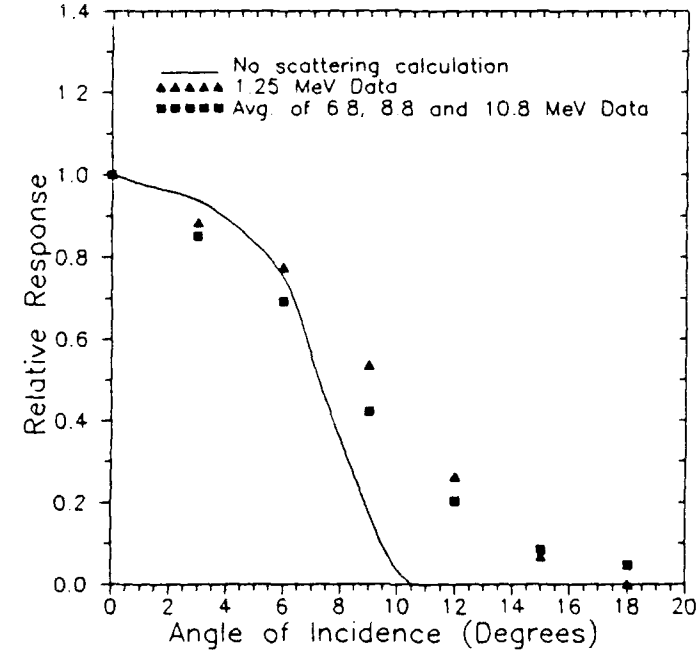

Figure 6 HEEF angular response to electrons (normalized to 1 at 0°).

It is clear that electron multiple scattering plays a significant role in the HEEF angular response, as the low energy distribution is broader than the high energy distribution and both are broader than the distribution calculated assuming no electron scattering. In practice, the effective geometric factor at a given energy E was extracted from the data using the measured 0° effective area and a smooth cubic spline function fit to the measured $f(E,\Theta)$ values. For the RADC data at 6.8, 8.8 and 10.8 MeV the average of the three angular distributions was used. The RADC angular distributions at lower energies were extremely (and un-physically) broad. This was due to the severe angular scattering of the beam electrons in the beam pipe exit window and in air. As a result those angular distributions could not be used in eq. (4.5). Instead, the following procedure was followed. For the 1.3 and 1.8 MeV data points, the angular distributions of the closest GSFC data runs (1.25 and 1.75 MeV) were used. For the remaining data points, the average of the high energy distributions was used. The experimental values of the effective geometric factors are listed in Table 3 and are plotted (new GF) in Figure 7. The old GF values are those quoted in Ref. 1. The coefficients of the fit polynomial are listed in Table 4.

Table 3 Effective HEEF 0° Area and Geometric Factors.

Energy (MeV)	Test	A(E,0°) (10^{-4} cm^2)	Geometric Factor (10^{-5} cm^2-sr)
1.00	GSFC	1.5	1.4
1.25	GSFC	20.0	18.5
1.30	RADC	26.9	24.9
1.50	GSFC	49.4	72.1
1.75	GSFC	81.3	113
1.80	RADC	76.1	106
2.30	RADC	98.9	134
2.80	RADC	169	221
3.30	RADC	243	305
3.80	RADC	336	403
4.20	RADC	258	298
6.80	RADC	936	796
8.80	RADC	771	655
10.80	RADC	1325	1149

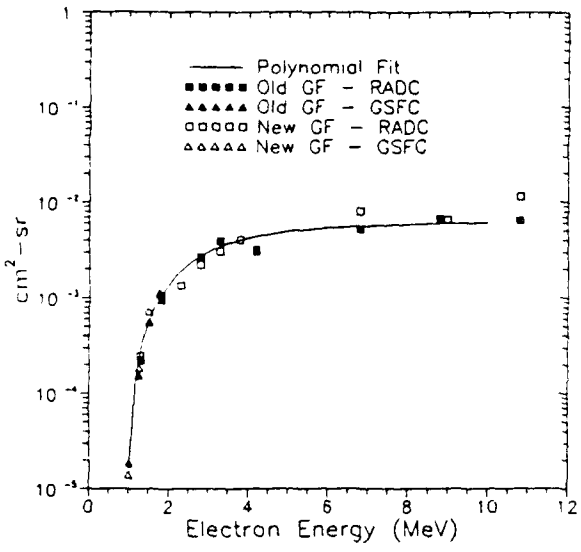

Figure 7 Effective HEEF geometric factors.

Table 4 Coefficients for a polynomial fit to GF(E).

$$GF(E) = \Sigma\, C_i \cdot E^i$$

i	C_i
0	0.00229551
1	-0.007063260
2	0.00740881
3	-0.003476120
4	0.00103210
5	-0.000205743
6	$2.70496 \cdot 10^{-5}$
7	$-2.22341 \cdot 10^{-6}$
8	$1.02801 \cdot 10^{-7}$
9	$-2.03266 \cdot 10^{-9}$

4.3.3 Channel Effective Geometric Factors

The effective geometric factor for a given differential energy channel (ex: LL-L1 or L5-L6) is given by

$$GF(Ln) = 2\pi \int dE\, R(E, L_n)\, A(E, 0°) \int d\theta\, f(E,\theta) \sin(\theta) \qquad (4.6)$$

where $R(E,L_n)$ is the probability that an electron with energy E will deposit an amount of energy in the BGO crystal within the limits of channel L_{n-1}-L_n. For an ideal detector, the function $R(E,L_n)$ would be 1 for all energies between the limits of the channel energy range, as given in Table 2, and 0 otherwise. Energy straggling in the solid state detectors and the BGO crystal energy resolution will modify the ideal $R(E,L_n)$ function. The theoretically expected form of $R(E,L_n)$, with parameters determined by the known electron straggling data and BGO crystal resolution, is (Ref. 1)

$$R(E, L_n) = \begin{cases} M_n \exp\left(-(E-P_n^-)^2/2\sigma^2\right) & \text{if } E < P_n^- \\ M_n & \text{if } P_n^- \le E \le P_n^+ \\ M_n \exp\left(-(E-P_n^+)^2/2\sigma^2\right) & \text{if } E > P_n^+ \end{cases} \qquad (4.7)$$

where $P_n^{\pm} = P_n \pm \delta P_n$. The physical significance of the parameters in eq. (4.7) is as follows: P_n is the central energy of the channel, M_n is the relative channel geometric factor at $E = P_n$, δP_n is the half width over which $R(E,L_n) = M_n$ and σ_n is the edge falloff width. Values of the parameters in eq. (4.7) are listed in Table 5. Effective channel geometric factors, calculated using eqs. (4.6) and (4.7) are listed in Table 2.

It is not possible to directly compare the $GF(L_n)$ values from Table 2 with either measured values or values calculated using the results of presently available TIGER code calculations. The measured BGO high energy spectra were obtained using electron beams that were not mono-energetic but had traversed a large amount of material and, therefore, suffered energy losses and energy straggling. TIGER calculations did not require coincidences between the detectors so that calculated BGO crystal electron spectra included some counts due to particles that would not have properly triggered the triple coincidence logic. Despite these limitations, it is still instructive to examine the measured and TIGER code derived BGO crystal energy spectra and consider what their shapes imply for the tabulated $GF(L_n)$ values.

BGO crystal pulse height spectra, measured at RADC and calculated using the TIGER code are shown in Figures 8 and 9. Despite the limitations outlined above, there is good agreement between the measured and calculated spectra. The key feature of the spectra is the small size of the low energy tail (low energy channel counts). Counts in the low energy tail are

high energy electrons misidentified as low energy electrons. TIGER code predicts no more than 30-40% of the total counts to be in the tail, while the RADC measurements give a value of about 15%. Both numbers are upper limits, the TIGER code value because detector coincidences were not implemented in the calculation, and the RADC value because the electron beam had a real low energy tail due to scattering in the beam pipe exit window. The small size of the low energy tail implies that high energy electron counts are not removed in significant quantities from the high energy channels and placed erroneously in the low energy ones.

The spectra in Figures 8 and 9 imply a poorer energy resolution than that predicted by eq. (4.7). The effect of this would be to remove some counts from the proper energy channel and place them in the next lower one. It is not clear, however, whether the observed, poorer energy resolution is not simply due to the limitations of the TIGER code calculations and the energy losses and straggling of the RADC beams. Final resolution of this question will await improved TIGER code calculations and the possible calibration of the HEEF sister instrument with high quality, high energy electron beams.

The electron spectrum in the radiation belts falls off rapidly with increasing energy, so that removing a small fraction of high energy counts and moving them to a lower energy channel lowers the higher energy channel count but does not appreciably increase the lower energy channel count. Thus, the combined effect of the low energy tail and lower energy resolution would be to decrease the quoted channel geometric factors. Based on measurements and calculations, it appears that this decrease is of the order of 20% or less.

Table 5 Parameter values for eq. (4.7).

Channel	M_n	P_n (MeV)	δP_n (MeV)	σ_n (MeV)
LL-L1	0.919	1.30	0.00	0.234
L1-L2	0.914	1.82	0.00	0.234
L2-L3	0.925	2.35	0.00	0.234
L3-L4	0.896	2.80	0.00	0.221
L4-L5	0.886	3.30	0.00	0.234
L5-L6	0.905	3.80	0.00	0.221
L6-L7	0.997	4.55	0.15	0.293
L7-L8	0.997	5.55	0.15	0.340
L9-L9	1.000	7.08	0.58	0.357
L9-L10	1.000	9.05	0.50	0.425

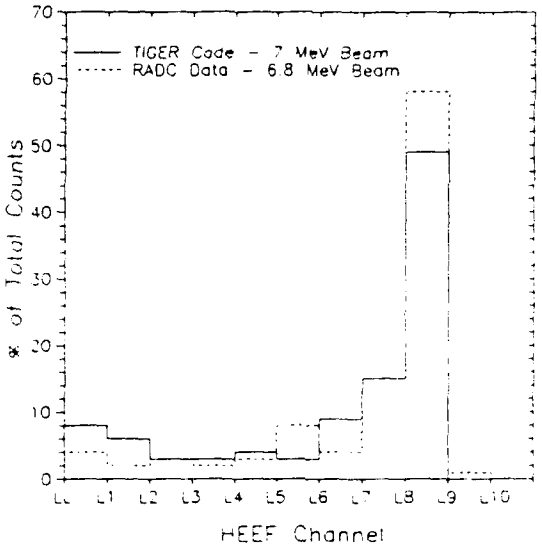

Figure 8 BGO crystal pulse height spectra.

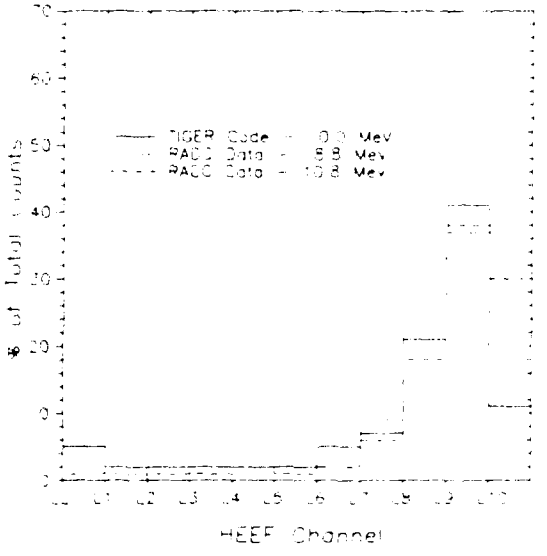

Figure 9 BGO crystal pulse height spectra.

4.3.4 Temperature and High Voltage Effects

HEEF was calibrated at a high voltage step HV=128 (voltage of the photomultiplier viewing the BGO crystal) and at room temperature, +20 °C. The typical on-orbit operating HEEF temperature, however, has ranged from 0 to -10 °C, with the majority of time being spent near the -10 °C mark. In addition, HEEF was erroneously put into a HV=192 high voltage step during orbit 276 and stayed in that state until orbit 355, when a scheduled instrument OFF/ON cycle resulted in resetting the high voltage to the HV=128 step. This section describes the effects of HV step and temperature changes on HEEF data.

The variation of light output from the BGO scintillator been reported in literature to be of the order of -1.5%/°C (decreasing with increasing temperature). The PMT gain, on the other hand increases with temperature thus counteracting the BGO effect to some extent. Data taken with HEEF show that the instrument gain as a function of temperature, G_T, can be written as:

$$G_T = 1.122 - 6.093 \cdot 10^{-3} T \qquad (4.8)$$

where T is in °C and the gain at +20 °C is taken to be unity. This corresponds to a gain change of ≈ -0.7 %/°C. The variation of electronic thresholds (LL, L1, ... L10) with temperature is very slight. Typical threshold variation is < -0.1%/°C. This is much smaller than the gain variation of the BGO crystal and can be neglected in comparison to it.

The BGO crystal photomultiplier high voltage can be set from 1070 Volts (HV_{step} = 0) to 1305 Volts (HV_{step} = 255). One high voltage step corresponds to approximately 0.92 Volts. Linear extrapolation of data, taken at +20 and +40 °C, gives the gain variation with HV step, G_{HV}, as:

$$G_{HV} = 0.56 + 3.438 \cdot 10^{-3} HV_{step} \qquad (4.9)$$

where HV_{step} is between 0 and 255 and $G_{128} \equiv 1$. The combined effect of temperature and HV_{step} on the system gain (relative to the fixed electronic thresholds), $G(HV_{step},T)$, can be expressed as:

$$G(HV_{step}, T) = -2.095 \cdot 10^{-5} HV_{step} T - 3.412 \cdot 10^{-3} T + 3.857 \cdot 10^{-3} HV_{step} + 0.628 \qquad (4.10)$$

with T and HV_{step} as defined above.

HEEF data are affected by a gain shift in two ways: 1) the electron energies corresponding to the LL through L10 thresholds change and 2) the effective geometric factors of the electron channels change. The electron energy corresponding to a channel threshold, $E(Ln,HV_{step},T)$, is given by:

$$E(L_n, HV_{step}, T) = \frac{E_o(L_n)}{G(HV_{step}, T)} \qquad (4.11)$$

where $E_o(Ln)$ are the nominal (+20 °C, HV_{step} = 128) channel energy thresholds, as given in Table 2, and $G(HV_{step},T)$ is the gain as a function of temperature and high voltage eq. (4.10)). The effective n^{th} channel geometric factor, $GF_n(T,V)$, is given by:

$$GF_n(HV_{step}, T) = \int_0^{\infty} GF(E) \cdot R(E'(HV_{step}, T), L_n)\, dE \qquad (4.12)$$

where GF(E) is the effective HEEF geometric factor, given by eq. (4.5), and $R(E,L_n)$ is the channel energy response function, eq. (4.7) and $E'(HV_{step},T) = E \cdot G(HV_{step},T)$. Table 6 contains a listing of channel limits and geometric factors for the most commonly occurring HEEF voltage and temperature conditions.

Table 6 Effective channel geometric factors and energy limits for selected values of HEEF temperature and HV_{step} (geometric factors are in cm^2-sr-keV, limits in MeV)

	T=0 °C HV=128		T=-10 °C HV=128		T=-10 °C HV=192	
Channel	Limits	Eff. GF	Limits	Eff. GF	Limits	Eff. GF
LL-L1	0.89-1.34	0.092	0.85-1.27	0.063	0.69-1.04	0.010
L1-L2	1.34-1.78	0.372	1.27-1.69	0.295	1.04-1.39	0.102
L2-L3	1.78-2.23	0.755	1.69-2.11	0.632	1.39-1.73	0.294
L3-L4	2.23-2.67	0.990	2.11-2.54	0.849	1.73-2.08	0.446
L4-L5	2.67-3.12	1.358	2.54-2.96	1.188	2.08-2.43	0.680
L5-L6	3.12-3.57	1.582	2.96-3.38	1.405	2.43-2.77	0.855
L6-L7	3.57-4.46	3.905	3.38-4.23	3.529	2.77-3.47	2.306
L7-L8	4.46-5.35	5.002	4.23-5.07	4.600	3.47-4.16	3.224
L8-L9	5.35-7.13	9.915	5.07-6.76	9.226	4.16-5.54	6.907
L9-L10	7.13-8.92	10.727	6.76-8.46	10.043	5.54-6.93	7.736

5. SUMMARY AND CONCLUSIONS

An extensive effort has been made to re-analyze the HEEF calibration data and remove some of the deficiencies due to poor beam quality at one of the calibration facilities (RADC). In addition, a computer model of the HEEF response to electrons, utilizing the TIGER electron transport code, has been developed, and model calculation results have been compared to the data. The agreement between the data and the calculation results is very good. The new calibration results are in excellent agreement, to within the experimental accuracy, with the results previously quoted in Ref. 1. There is a possibility that the quoted geometric factors are slightly high (by 20% or less). This possibility will be further investigated.

REFERENCES

1) B. K. Dichter and F. A. Hanser, "Development and Use of Data Analysis Procedures for the CRRES Payloads AFGL-701-2/Dosimeter and AFGL-701-4/Fluxmeter and Application of the Data Analysis Results to Improve the Static and Dynamic Models of the Earth's Radiation Belts," GL-TR-89-0284, Phillips Laboratory, Geophysics Directorate, Hanscom AFB, MA, October 1989 (ADA219479).

2) J. L. Hunerwadel, B. Sellers and F. A. Hanser, "Design, Fabricate, Calibrate, Test and Deliver Two Satellite Electron Flux Detectors," AFGL-TR-87-0205, Phillips Laboratory, Geophysics Directorate, Hanscom AFB, MA, June 1987 (ADA190799).

3) The authors gratefully acknowledge Dr. W. Cottingame and A. Mioduszewski of Los Alamos National Laboratory for their help in running the TIGER code.